PHYSICAL REVIEW FLUIDS **9**, 024601 (2024)

Turbulent puffs in transitional pulsatile pipe flow at moderate pulsation amplitudes

Daniel Morón
Center of Applied Space Technology and Microgravity (ZARM), University of Bremen,
Am Fallturm 2, 28359 Bremen, Germany

Marc Avila
Center of Applied Space Technology and Microgravity (ZARM), University of Bremen,
Am Fallturm 2, 28359 Bremen, Germany
and MAPEX Center for Materials and Processes, University of Bremen,
Am Biologischen Garten 2, 28359 Bremen, Germany

(Received 12 October 2023; accepted 4 January 2024; published 8 February 2024)

We show that, in the transitional regime of pulsatile pipe flow, at moderate-to-high amplitudes $0.5 \lesssim A \lesssim 1$, the first long-lived turbulent structures are localized and take the form of the puffs and slugs observed in statistically steady pipe flow. We perform direct numerical simulations at many pulsation frequencies (Wo), amplitudes, and Reynolds number (Re) and observe different dynamics of puffs and slugs. At certain flow parameters we find, using a causal analysis, that puffs actively make use of linear instabilities in the laminar Sexl-Womersley (SW) profile to survive the pulsation. Using all these lessons learned, we extend a low-order model by Barkley *et al.* [Nature (London) **526**, 550 (2015)] to reproduce these dynamics. We find a good agreement between the extended model and our numerical results in a broad parametric space of pulsation amplitudes $0.5 \lesssim A \lesssim 1$, frequencies $\mathrm{Wo} \gtrsim 5$ and $2100 \leqslant \mathrm{Re} \leqslant 3000$. With the help of our numerical results, causal analysis and model, we determine that turbulence production has two sources at these flow parameters: the mean shear as in statistically steady pipe flow and the instabilities of the instantaneous pulsatile mean profile.

DOI: 10.1103/PhysRevFluids.9.024601

I. INTRODUCTION

More than a century after Reynolds experiments [1], we are closer to fully understand turbulence transition in statistically steady pipe flow (SSPF), see Avila *et al.* [2] for a recent review. For sufficiently perturbed flows, transition only depends on the Reynolds number $\mathrm{Re} = UD/\nu$, where U is the time-averaged bulk velocity, D the diameter of the pipe, and ν the kinematic viscosity of the fluid. Despite being linearly stable, at least up to $\mathrm{Re} \leqslant 10^7$ [3], perturbations in SSPF can make use of nonmodal mechanisms to grow, saturate, and trigger turbulence at much lower $\mathrm{Re} \sim \mathcal{O}(10^3)$ [4]. The optimal perturbation, the one that attains a higher energy growth in SSPF, is a pair of streamwise vortices [5].

Once triggered, turbulence in SSPF first appears in the form of localized turbulent patches of constant length, known as turbulent puffs. Depending on the Reynolds number, puffs are more likely to either decay (at low $\mathrm{Re} \lesssim 2040$), split (at $2040 \lesssim \mathrm{Re} \lesssim 2250$), or elongate into slugs (at $\mathrm{Re} \gtrsim 2250$) [2]. Also depending on Re, puffs (slugs) move (and elongate) at a certain upstream (and downstream) front speed c_u (and c_d). The exact mechanisms by which turbulent puffs decay, split, or elongate are still unclear.

The low-order model proposed by Barkley *et al.* [6] (hereafter referred to as the Barkley model (BM) is able to reproduce the front speeds of turbulent puffs and slugs in SSPF. In this paper we provide a description of the model in Appendix B. The reader is referred to Barkley [7] and references therein for a more detailed description. In short, the model considers only two one-dimensional, time-dependent variables, $q(x, t)$ and $u(x, t)$, whose evolution is described by two nonlinearly coupled advection-diffusion-reaction equations. These equations are inspired by, but not derived from, the Navier-Stokes equations. In fact, the variables and the parameters represent features of pipe flow but have arbitrary physical units. The variable q represents the turbulence intensity, and u the state of the local mean shear of the flow, at each axial location x and time t. The key feature of the BM is the nonlinear interaction between u and q. The turbulence intensity q takes advantage of the mean shear u to grow. However, in the axial locations where $q > 0$, the local mean shear is reduced [8], and in turn, adversely affects the growth of q. When fitted correctly, the model returns the turbulent front speeds c_u and c_d of turbulent structures in SSPF with high accuracy in a broad Re regime [6,9,10]. The remarkable success of this model has motivated some researchers to use it to study puff split dynamics [11] or even turbulence transition of non-Newtonian pipe flow [12]. The question still remains to what extent the assumptions and simplifications of the BM are correct and if it can be easily adapted to similar flow setups, such us pipe flows driven at an unsteady flow rate.

We study pulsatile pipe flows, whose bulk velocity $\bar{U}(t)$ has one harmonic component:

$$\bar{U}(t) = U[1 + A\sin(2\pi f t)]. \tag{1}$$

The flow depends on three parameters: the mean Re, the frequency of the pulsation $f = 1/T$ or its nondimensional counterpart, the Womersley number $\mathrm{Wo} = D/2\sqrt{2\pi f/\nu}$, and the amplitude A. In the case of smooth rigid pipes, considered here, there is an analytical solution to laminar pulsatile pipe flow, the Sexl-Womersley (SW) profile $U_{\mathrm{SW}}(r, t)$ [13,14].

At small-to-moderate amplitudes $A \leqslant 0.4$ and transitional $\mathrm{Re} \approx 2000$, the first long-lived turbulent structures found in pulsatile pipe flows are also turbulent puffs [15]. Their behavior depends on the pulsation frequency. At high $\mathrm{Wo} \gtrsim 20$ (independently of A) puffs do not have enough time to adapt to the fast harmonic driving [16], and their behavior is identical to the one found in SSPF. At low $\mathrm{Wo} \lesssim 4$ the behavior is quasisteady, and the puff dynamics depend on the instantaneous Reynolds number $\mathrm{Re}_i(t) = \frac{\bar{U}(t)}{U}\mathrm{Re}$ [15]. At intermediate $5 \lesssim \mathrm{Wo} \lesssim 19$, the behavior of puffs smoothly transitions between the two limiting cases described above. It is still unclear whether this also happens at $A \geqslant 0.5$.

At moderate-to-large amplitudes $0.5 \leqslant A \leqslant 1$, $\mathrm{Re} \approx 2000$, and intermediate frequencies, $5 \lesssim \mathrm{Wo} \lesssim 19$, the SW profile is instantaneously unstable at some phases of the pulsation period [17]. This instability is linked to the presence and behavior of inflection points in the laminar profile [18,19]. Helical perturbations can take advantage of this instability to grow, and trigger turbulence, as first reported by Xu *et al.* [20]. At these flow parameters, although the optimal perturbation of SSPF, the pair of streamwise vortices, can substantially grow in energy, helical perturbations exhibit the maximum growth [21–23], consistent with experiments [20]. In direct numerical simulations (DNS), helical perturbations rapidly grow, saturate, and trigger turbulence that, at some flow parameters, takes the form of localized puffs modulated in length and magnitude by the pulsation [17]. Recent results suggest that these turbulent puffs actively make use of the instantaneous instabilities of the SW profile to survive during the phases of the period when $\mathrm{Re}_i(t)$ is too low [24]. This hypothesis, however, has not been rigorously verified yet.

In this paper, we study turbulent puffs in transitional pulsatile pipe flow at $2100 \leqslant \mathrm{Re} \leqslant 3000$, moderate-to-large amplitudes $0.5 \leqslant A \leqslant 1$, and intermediate frequencies $5 \lesssim \mathrm{Wo} \lesssim 19$. We perform DNS at many Re, Wo, and A and study the behavior of turbulent puffs at these flow regimes. We perform causal analyses to determine if they make use of the instabilities of the laminar profile to survive the pulsation, as suggested by Feldmann *et al.* [24]. Using the lessons learned from these analyses, we extend the BM to a new extended Barkley model (EBM) that reproduces the dynamics of turbulent puffs in pulsatile pipe flow throughout the parameter regime studied in the DNS.

The paper is organized as follows. In Sec. II we describe the numerical methods we use to perform DNS of pulsatile pipe flow. In Sec. III, we analyze our DNS results of pulsatile pipe flows at several flow parameters. In Sec. IV, we present the results of our causal analysis and in Sec. V the comparison between the extended model and DNS results. Finally, in Sec. VI we draw some conclusions.

II. METHODS

We consider a viscous Newtonian fluid with constant properties in a straight smooth rigid pipe of circular cross section, with a time-dependent bulk velocity, Eq. (1). The flow is assumed to be incompressible and governed by the dimensionless Navier-Stokes equations (NSE):

$$\frac{\partial \vec{u}}{\partial t} + (\vec{u}\cdot\nabla)\vec{u} = -\nabla p + \frac{1}{\mathrm{Re}}\nabla^2\vec{u} + P_G(t)\vec{e}_x \quad \text{and} \quad \nabla\cdot\vec{u} = 0. \tag{2}$$

Here $\vec{u}$ is the fluid velocity, p the pressure, and P_G the time-dependent axial pressure gradient which drives the flow at the bulk velocity defined in Eq. (1). All variables in this study are rendered dimensionless using the pipe diameter (D), the time-averaged bulk velocity (U), and the fluid density (ρ_f).

A. Computational methods

We perform direct numerical simulations of Eq. (2) using our open-source pseudospectral simulation code `nsPipe` [25]. In `nsPipe`, the governing equations are discretized in cylindrical coordinates (r, θ, x) using a Fourier-Galerkin ansatz in θ, with wave number $m \in \mathbb{Z}$, and x with wave number $\alpha = \alpha_0 k$. Here $\alpha_0 = 2\pi/L$, where L is the pipe length and $k \in \mathbb{Z}$. We use high-order finite differences in r with stencils of length 7 for master-slave simulations (see Sec. IV) and of length 9 in individual DNS simulations. Periodic boundary conditions are imposed in θ and x and no-slip boundary conditions in the solid pipe wall. The discretized NSE are integrated forward in time using a second-order predictor-corrector method with variable time-step size (Δt) as in `openpipeflow` [26]. Further details about the implementation of `nsPipe` are given in López *et al.* [25] and references therein.

We perform single DNS of pulsatile pipe flow at different Re, Wo, and A. See the parameters of all our simulations at the end of the paper, in Table I. The time-step size is always $\Delta t < 0.0025D/U$, the length of the pipe is $L = 100D$, and the simulation with the coarsest grid in terms of + units has $0.044 \leqslant \Delta r^+ \leqslant 2.39$, $D^+\Delta\theta/2 = 4.08$, and $\Delta x^+ = 8.27$. We initialize the simulations with the corresponding SW profile in the whole domain. We trigger a single turbulent puff in each simulation by introducing the corresponding optimal perturbation localized in a $5D$ axial section of the pipe and scaled to $|\mathbf{u}_0'| \approx 3 \times 10^{-2}$, following Feldmann *et al.* [24] and Morón *et al.* [17]. We compute the optimal perturbation using a transient growth analysis (TGA). The reader is referred to Xu *et al.* [21] and Morón *et al.* [17] for more details on the transient growth analysis.

B. Averages

We compute averages of the three velocity components u_r, u_θ, and u_x and the axial (streamwise) vorticity ω_x. Angled brackets $\langle\bullet\rangle_\psi$ denote averaging with respect to ψ, where ψ denotes one or more variables. Spatial averages are performed with respect to one or more coordinates: radial $\psi \equiv r$, azimuthal $\psi \equiv \theta$, and axial $\psi \equiv x$. Temporal averages are performed using the whole time series and are denoted with $\psi \equiv t$. Ensemble averages, using N_i individual simulations, are denoted with $\psi \equiv N_i$. Phase averages correspond to averaging at several phases of the period and are denoted as $\psi \equiv t^*$. In the latter case, we split the pulsation period in 200 equispaced period phases and we perform averages at each of them. The resulting signal is phase (t^*) but not time (t) dependent.

TABLE I. Simulations in a $L = 100D$ long pipe of pulsatile pipe flow performed in this study. Columns show the identification number of the simulation (Case); the flow parameters (Re, Wo, and A); the radial points N_r and half the number of azimuthal and axial Fourier modes N_θ and N_x (the total number of physical points is $N_r \times 3N_\theta \times 3N_x$); the maximum Re_τ and grid discretization in + units; the total number of periods run in the simulation NT and the behavior of the simulation according to the description in Sec. III: rapid decay (RaD), localized structures (Loc), stochastic decay (StD), and highly intermittent state (Int).

Case	Re	Wo	A	N_r	N_θ	N_x	Re_τ	$\Delta r^+_{\mathrm{min}}$	$\Delta r^+_{\mathrm{max}}$	$\Delta R\theta^+$	Δx^+	NT	Behavior
1	2100	8	0.50	96	80	1200	96.49	0.022	1.47	2.53	5.36	8.3	StD
2	2100	9	0.50	96	96	1600	99.52	0.023	1.52	2.17	4.15	12.4	Loc
3	2100	9	1.00	96	96	1536	123.55	0.028	1.89	2.70	5.36	23.0	StD
4	2100	11	0.50	96	80	1800	104.68	0.024	1.60	2.74	3.88	188.0	Loc
5	2100	11	0.75	96	80	1800	118.75	0.027	1.81	3.11	4.40	7.9	Loc
6	2100	11	1.00	96	80	1800	131.87	0.030	2.01	3.45	4.88	193.0	Loc
7	2100	15	0.50	96	80	1800	114.92	0.026	1.75	3.01	4.26	10.0	Loc
8	2100	15	1.00	96	80	1800	146.73	0.034	2.24	3.84	5.43	64.0	Loc
9	2100	17	0.50	96	80	1800	118.95	0.027	1.82	3.11	4.41	10.0	Loc
10	2100	17	1.00	96	80	1800	153.99	0.035	2.35	4.03	5.70	10.0	Loc
11	2200	5	0.50	96	80	1200	88.74	0.020	1.35	2.32	4.93	3.2	RaD
12	2200	8	0.50	96	80	1200	98.89	0.023	1.51	2.59	5.49	7.4	Loc
13	2200	8	1.00	96	80	1200	121.18	0.028	1.85	3.17	6.73	2.9	RaD
14	2200	9	0.50	96	80	1200	101.89	0.023	1.56	2.67	5.66	10.7	Loc
15	2200	11	0.50	96	96	1800	107.44	0.025	1.64	2.34	3.98	36.7	Loc
16	2200	11	1.00	96	96	1800	134.95	0.031	2.06	2.94	5.00	35.0	Loc
17	2400	8	0.50	96	96	2400	103.90	0.024	1.59	2.27	2.89	5.9	Loc
18	2400	8	1.00	96	96	2400	127.39	0.029	1.94	2.78	3.54	3.8	RaD
19	2500	8	1.00	96	80	1200	129.36	0.030	1.97	3.39	7.19	1.7	RaD
20	2500	9	1.00	96	80	1200	137.43	0.031	2.10	3.60	7.63	10.8	Int
21	2500	11	1.00	96	80	1200	147.43	0.034	2.25	3.86	8.19	12.5	Int
22	2600	8	1.00	96	80	1200	132.19	0.030	2.02	3.46	7.34	2.8	StD
23	2600	11	1.00	96	80	1200	148.81	0.034	2.27	3.90	8.27	11.6	Int
24	2700	8	1.00	128	96	1536	134.57	0.017	1.55	2.94	5.84	1.8	RaD
25	2700	9	1.00	128	96	1536	144.27	0.019	1.66	3.15	6.26	8.7	Int
26	2700	11	1.00	128	96	1536	154.13	0.020	1.77	3.36	6.69	9.2	Int
27	2800	8	1.00	128	96	1536	136.94	0.018	1.57	2.99	5.94	2.6	RaD
28	2800	11	1.00	128	96	1536	159.07	0.021	1.83	3.47	6.90	9.2	Int
29	2900	8	1.00	128	96	1536	143.55	0.019	1.65	3.13	6.23	6.5	Loc
30	2900	9	1.00	128	96	1536	150.14	0.019	1.73	3.28	6.52	8.3	Int
31	2900	11	1.00	128	96	1536	161.83	0.021	1.86	3.53	7.02	8.5	Int
32	3000	6	0.50	128	128	1536	114.48	0.015	1.32	1.87	4.97	3.5	Loc
33	3000	6	1.00	128	96	1536	129.97	0.017	1.49	2.84	5.64	1.5	RaD
34	3000	8	0.50	128	96	1536	118.80	0.015	1.37	2.59	5.16	4.0	Int
35	3000	8	1.00	128	96	1536	143.27	0.019	1.65	3.13	6.22	4.9	StD
36	3000	11	0.50	96	96	2800	136.95	0.031	2.09	2.99	3.26	4.6	Int
37	3000	11	1.00	128	96	1536	166.88	0.022	1.92	3.64	7.24	4.4	Int

III. DNS RESULTS

We perform DNS of pulsatile pipe flow at different combinations of $\mathrm{Re} \geqslant 2100$, $5 \leqslant \mathrm{Wo} \leqslant 19$, and $0.5 \leqslant A \leqslant 1$. At these flow parameters, turbulence always takes the form of localized turbulent puffs that are modulated by the pulsation, as shown in Fig. 1. See a list of the DNS we analyze here at the end of the paper in Tables I and II.

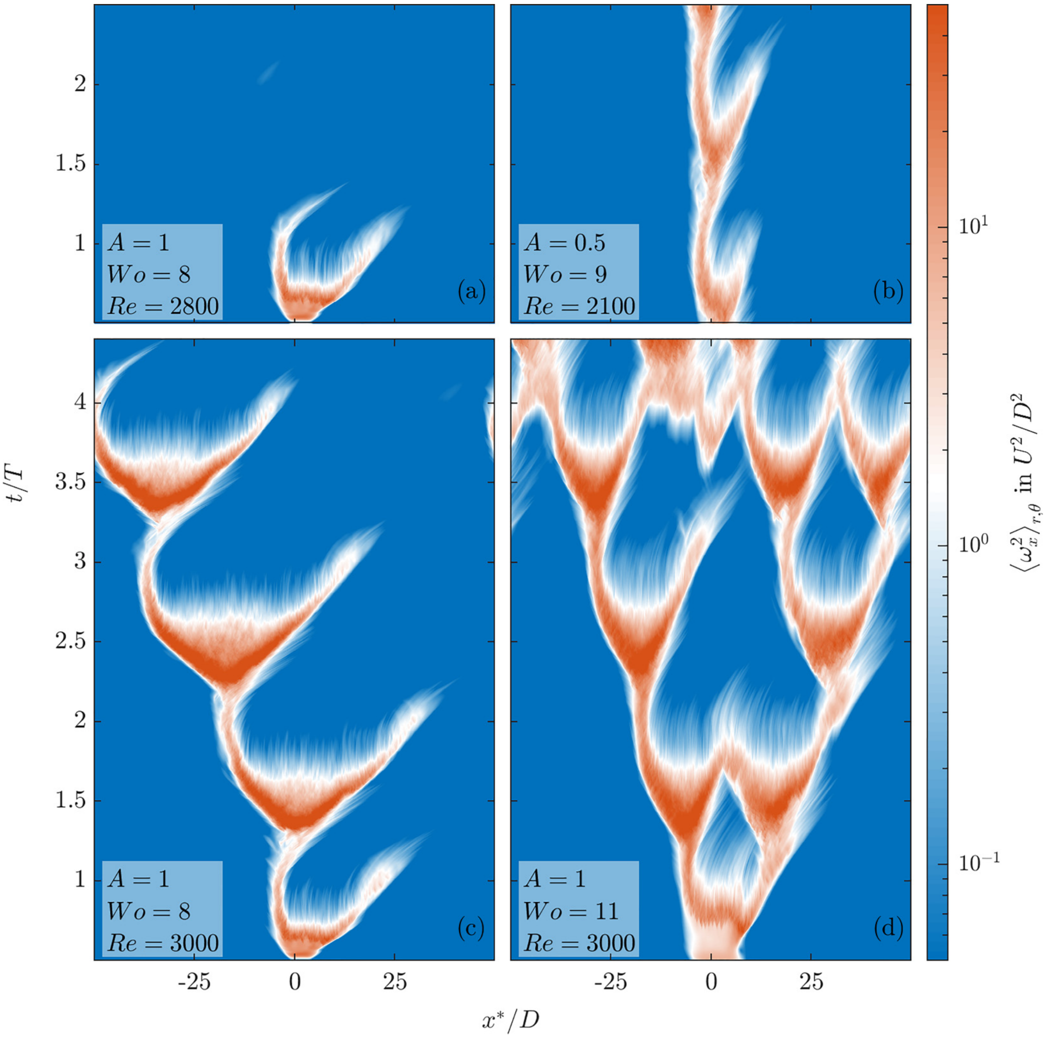

FIG. 1. Space-time diagrams of the cross-section integral of axial vorticity squared $\langle\omega_x^2\rangle_{r,\theta}$ of DNS in a 100D long pipe at different flow parameters. The DNS are initialized with the optimal perturbation scaled to $|\mathbf{u}_0'| \approx 3 \times 10^{-2}$ of magnitude and localized in an axial span of 5D following Feldmann *et al.* [24]. The results are shown with respect to a noninertial reference frame $x^*(t) = \int_0^t \bar{U}(t')dt'$, moving with the bulk velocity $\bar{U}(t)$.

In the parametric space considered here, we observe four different behaviors of turbulent puffs. We classify our DNS according to these four behaviors (see Tables I and II):

(1) *First elongation and then rapid decay (RaD)*: The initial helical perturbation, used to initialize the flow, first grows in length and magnitude and then decays in less than one pulsation period [Fig. 1(a)]. We classify these decay events as deterministic. They are different from decay events that happen (stochastically) after more than one pulsation period, which we classify in another category (3 below).

(2) *Localized turbulent structures (Loc)*: The initial helical perturbation localizes in a puff, that is then modulated in length and magnitude by the pulsation and survives for long times without splitting or decaying. See an example of this behavior in Fig. 1(b).

TABLE II. Simulations of pulsatile pipe flow using the master-slave method described in Sec. IV performed in this study. All the simulations correspond to a $L = 100D$ long pipe. In columns find the identification number of the simulation (Case); the flow parameters (Re, Wo, and A); the radial points N_r and half the number of azimuthal and axial Fourier modes N_θ and N_x (the total number of physical points is $N_r \times 3N_\theta \times 3N_x$); the maximum Re_τ and grid discretization in + units; the total number of periods run in the simulation NT and the behavior of the master simulation according to the description in Sec. III: rapid decay (RaD), localized structures (Loc), stochastic decay (StD), and highly intermittent state (Int).

Case	Re	Wo	A	N_r	N_θ	N_x	Re_τ	$\Delta r^+_{\mathrm{min}}$	$\Delta r^+_{\mathrm{max}}$	$\Delta R\theta^+$	Δx^+	NT	Behavior
1	2100	9	0.50	80	64	1152	99.35	0.032	1.81	3.25	5.75	5.8	Loc
2	2100	9	0.70	80	64	1152	109.47	0.036	2.00	3.58	6.33	5.8	Loc
3	2100	9	0.90	80	64	1152	118.58	0.039	2.17	3.88	6.86	5.8	StD
4	2100	11	0.50	80	64	1152	104.55	0.034	1.91	3.42	6.05	6.0	Loc
5	2100	11	0.70	80	64	1152	116.35	0.038	2.12	3.81	6.73	7.8	Loc
6	2100	11	0.90	80	64	1152	126.71	0.041	2.31	4.15	7.33	6.0	Loc
7	2100	13	0.50	76	64	1152	109.68	0.039	2.10	3.59	6.35	9.6	Loc
8	2100	13	0.70	76	64	1152	122.38	0.044	2.35	4.01	7.08	9.6	Loc
9	2100	13	0.90	76	64	1152	133.99	0.048	2.57	4.38	7.75	9.6	Loc
10	2100	15	0.50	76	64	1152	114.47	0.041	2.19	3.75	6.62	13.6	Loc
11	2100	15	0.70	76	64	1152	128.50	0.046	2.46	4.21	7.44	13.6	Loc
12	2100	15	0.90	76	64	1152	140.92	0.051	2.70	4.61	8.16	13.6	Loc
13	2100	17	0.50	80	64	1152	119.02	0.039	2.17	3.89	6.89	11.0	Loc
14	2100	17	0.70	80	64	1152	134.08	0.044	2.45	4.39	7.76	11.0	Loc
15	2100	17	0.90	80	64	1152	147.39	0.048	2.69	4.82	8.53	11.0	Loc
16	2300	9	0.50	80	64	1152	104.52	0.034	1.91	3.42	6.05	4.8	Loc
17	2300	9	0.70	76	64	1152	114.97	0.041	2.20	3.76	6.65	4.8	Loc
18	2300	9	0.90	76	64	1152	124.75	0.045	2.39	4.08	7.22	4.8	StD
19	2300	11	0.50	80	64	1152	109.92	0.036	2.01	3.60	6.36	19.7	Loc
20	2300	11	0.70	80	64	1152	122.10	0.040	2.23	4.00	7.07	6.7	Loc
21	2300	11	0.90	80	64	1152	140.15	0.046	2.56	4.59	8.11	7.1	Loc
22	2300	13	0.50	80	64	1152	115.25	0.038	2.10	3.77	6.67	9.9	Loc
23	2300	13	0.70	80	64	1152	128.47	0.042	2.35	4.20	7.43	9.9	Loc
24	2300	13	0.90	80	64	1152	140.58	0.046	2.57	4.60	8.14	9.9	Loc
25	2300	15	0.50	80	64	1152	120.55	0.039	2.20	3.94	6.98	13.2	Int
26	2300	15	0.70	76	64	1152	134.89	0.048	2.59	4.41	7.81	13.2	Loc
27	2300	15	0.90	76	64	1152	148.14	0.053	2.84	4.85	8.57	14.8	Loc
28	2300	17	0.50	80	64	1152	125.86	0.041	2.30	4.12	7.28	20.0	Loc
29	2300	17	0.70	80	64	1152	141.07	0.046	2.58	4.62	8.16	20.0	Loc
30	2300	17	0.90	80	64	1152	154.80	0.050	2.83	5.07	8.96	16.0	Loc
31	2500	9	0.50	80	64	1152	109.47	0.036	2.00	3.58	6.34	4.9	Loc
32	2500	11	0.50	80	64	1152	115.18	0.038	2.10	3.77	6.67	5.8	Loc
33	2500	17	0.50	80	64	1152	133.98	0.044	2.45	4.38	7.75	17.5	Int
34	2500	17	0.70	80	64	1152	149.59	0.049	2.73	4.90	8.66	17.5	Int

(3) *Localized structures and then stochastic decay (StD)*: The initial helical perturbation localizes in structures that are modulated, in length and magnitude by the pulsation. These structures, however, tend to suddenly decay after typically a short number of pulsation periods [Fig. 1(c)]. Although we do not explicitly compute lifetime statistics of these cases here, these decay events happen at random times, as in pulsatile pipe flows at lower $A \leqslant 0.4$ [16] or driven with more complex waveforms [17]. In those analyses, the researchers report that turbulent structures decay after a random number of pulsation periods. However, different to SSPF, these decay events are more likely to happen at a particular phase of the period.

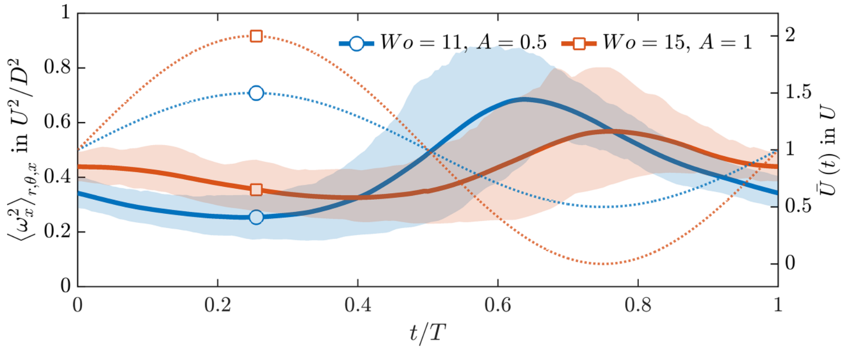

FIG. 2. Time profile of $\langle\omega_x^2\rangle_{r,\theta,x,t^*}$ (solid thick lines) compared with the bulk velocity $\bar{U}(t)$ (dotted lines) for Re = 2100, Wo, and A as indicated in the legend. The shaded regions delimit the volume of data between the max-min 10% percentile of the corresponding $\langle\omega_x^2\rangle_{r,\theta,x}(t^*)$ phase-dependent statistics.

(4) *Highly intermittent state (Int)*: The initial helical perturbation localizes in structures modulated by the pulsation. These structures, however, randomly split until the DNS reaches a highly intermittent state where turbulence aggregates in localized structures modulated by the pulsation and separated by laminar patches [Fig. 1(d)].

In the following section, Sec. IV, we study the mechanisms by which puffs are able to survive the pulsation at certain flow parameters. Here we briefly analyze the behavior of puffs in pulsatile pipe flow. We focus on two quantities, the upstream front speed of puffs c_u and the phase difference $\Delta\phi$, between the volume-averaged axial vorticity squared $\langle\omega_x^2\rangle_{r,\theta,x}(t)$ and the bulk velocity $\bar{U}(t)$. The former is the main observable that the results of the EBM are meant to approximate. The latter has to be considered in the EBM to correctly approximate the front speed of puffs, as shown in Sec. V and Appendix B.

We compute the upstream front speed c_u by tracking the upstream-most position in the turbulent puff, defined as $x_u = \min(u)$ such that $\langle\omega_x^2\rangle_{r,\theta} \geqslant 1 \times 10^{-1}$ for $x \gtrsim x_u$. We observe that the time signal of $\langle\omega_x^2\rangle_{r,\theta,x}(t)$ approximates a harmonic function, see Fig. 2, at all the flow parameters considered here. Thus, we compute the time-averaged phase difference $\langle\Delta\phi\rangle_t$ by projecting the time signal of $\langle\omega_x^2\rangle_{r,\theta,x}(t)$ to a harmonic function and comparing its phase with the sinusoidal bulk velocity. We repeat this for the data of all the simulations listed in Table I and the master DNS in Table II. We show the time-averaged upstream front speeds and phase difference of all the simulations together in Fig. 3.

We observe a phase difference between the turbulence intensity [represented by $\langle\omega_x^2\rangle_{r,\theta,x}(t)$] and bulk velocity consistent with studies of small-to-moderate amplitude $A \leqslant 0.4$ pulsatile pipe flow [16] and fully turbulent pulsatile channel flows [27]. There, they observed how the phase difference increases for increasing Wo, as we also observe in the cases considered here, see Fig. 3(a). At small Re $\approx$ 2100 the phase difference saturates at $\Delta\phi \approx \frac{3\pi}{2}$. There is no apparent effect of A on $\Delta\phi$.

The upstream front speed, as in the case of SSPF, is mainly affected by Re, see Fig. 3(b). The higher Re is, the smaller the upstream front speed becomes. According to our results, there is also a weak dependence of the front speed on A. The upstream front speed tends to decrease for increasing A. As Wo increases, the upstream front speed approximates the value of SSPF, as turbulence is less affected by the pulsation.

IV. MASTER-SLAVE CAUSAL ANALYSIS

Our hypothesis is that, as in SSPF [6,9,10], the behavior of puffs in pulsatile pipe flow is determined by the shape of the axial velocity profile $\langle u_x\rangle_\theta(x = x_u, r, t)$ at the upstream front $x \approx x_u$ of the puff. In the ideal case of an extremely long pipe, and a single localized turbulent puff, the

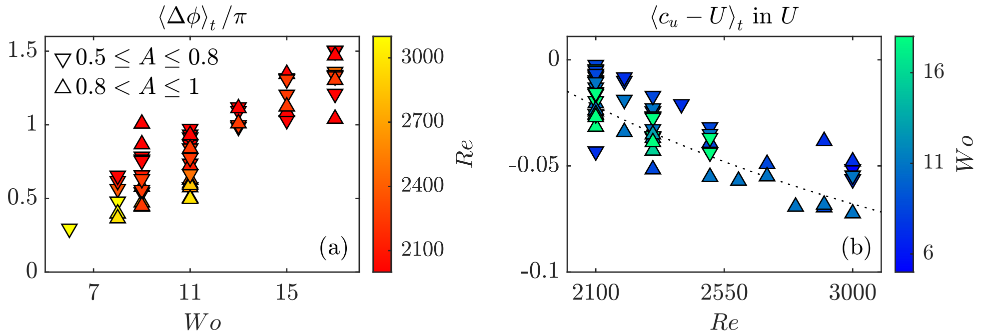

FIG. 3. Effect of flow parameters on (a) the phase difference $\Delta\phi$ between bulk velocity $\bar{U}$ and volume-averaged turbulence intensity $\langle \omega_x^2 \rangle_{r,\theta,x}(t)$ and (b) upstream front speed c_u. Each marker corresponds to the time-averaged value of either c_u or $\Delta\phi$ of an individual DNS of pulsatile pipe flow listed in Table I (and master simulations listed in Table II). Downward (upward) pointing triangles correspond to simulations at $0.5 \leqslant A \leqslant 0.8$ $(0.8 < A \leqslant 1)$. The face color indicates Re in (a) and Wo in(b). The dotted line in (b) corresponds to a fit of the upstream front speed of puffs in SSPF: $c_u - U \approx 0.28[0.024 + (\frac{\text{Re}}{1936})^{-0.528} - 1.06]$ in U, according to Chen *et al.* [10].

mean profile in the pipe $\langle u_x \rangle_{\theta,x}(r, t)$ approximates this profile. The idea is that puffs take advantage of two characteristics of the mean (upstream) velocity profile. One is the mean shear, as in SSPF, that, for the pulsatile case, is time dependent. The other is the instability of the SW profile that is linked with the presence of inflection points. We perform causal analysis of pulsatile pipe flow with the goal to separate the two mechanisms. Inspired by Tuerke and Jiménez [28], we perform DNS of pulsatile pipe flow with prescribed mean profiles in which inflection points are erased.

Following Vela-Martín [29] and references therein, we perform pairs of DNS that run in parallel to each other. In each pair, one of the simulations is a full DNS of pulsatile pipe flow, referred to as the master. The other simulation, referred to as the slave, uses the information of the master to modify some of its characteristics. Specifically, the slave simulation uses the instantaneous mean profile of the master $U_M = \langle u_x \rangle_{\theta,x}(r, t)$ to generate its instantaneous mean profile $U_S(r, t)$. A more detailed explanation of the methods used to compute $U_S(r, t)$ is given in the Appendix A.

We design time-dependent artificial (slave) profiles that, in the laminar case, have a shear that monotonically decreases from the center line to the pipe wall. Additionally, at each time step, the slave profiles have the same kinetic energy as the corresponding SW profile. See an example of the slave laminar profiles at Re = 2100, Wo = 11, and $A = 0.5$ in Figs. 4(a)–4(d). The slave profiles U_S have a similar magnitude to the actual SW profile, they are also time dependent but, different to the SW profile, they do not have inflection points.

A. Master-slave TGA

According to our hypothesis, the absence of inflection points prevents the outstanding transient growth of helical perturbations [17]. We test this hypothesis by performing TGA on the slave laminar profiles at many flow parameters and comparing the results with TGA on the corresponding SW profile. Note that, in the laminar case, the mean profile of the master is equal to the SW profile.

The TGA returns the shape (the radial profile and the axial α and azimuthal m wave number) of the infinitesimal perturbations that reach the highest energy growth G on top of a given flow profile. The TGA also returns the optimal time t_0 to trigger the perturbation and the final time t_f where perturbations reach the highest energy growth G. In this paper, we do not show the radial shape of the optimal perturbations, as our main interest is to check whether the slave profiles are highly susceptible to the growth of helical perturbations with $\alpha > 0$ and $m = 1$ or not. We also do not analyze t_f or the optimal time to trigger the perturbations, which is always around $t_0 \approx T/2$

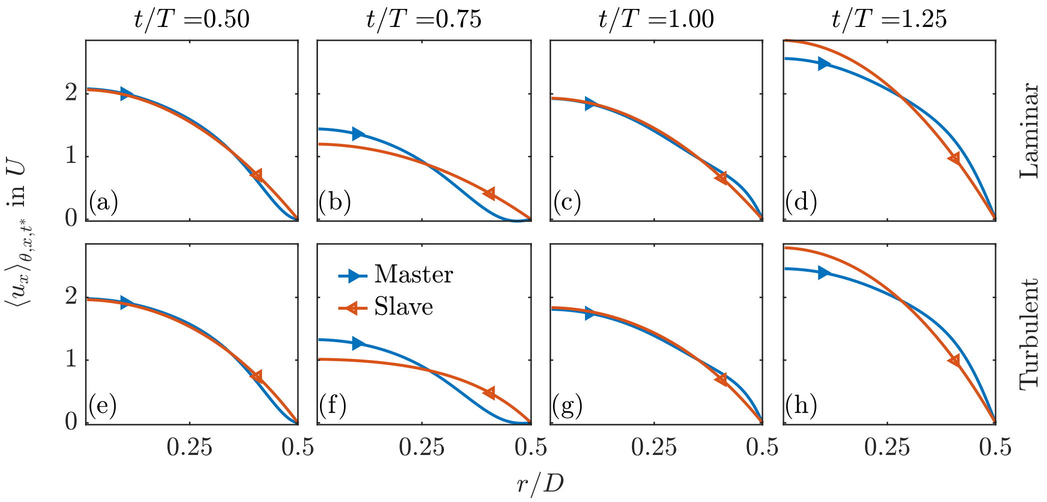

FIG. 4. Phase- (t^*) averaged mean profiles of master (M) and slave (S) simulations at Re = 2100, Wo = 11, and $A = 0.5$ for the case of fully laminar [(a)–(d)] and turbulent flows [(e)–(h)]. The phase of the period is indicated at the top of each subplot column.

[21]. We report the maximum transient growth we observe at any point in time during one pulsation period $t_f - t_0 \leqslant T$. We plot as colormaps the results of our TGA in Fig. 5.

We perform two different TGA of our laminar (SW) master profiles. In the first TGA, we consider all possible perturbations with $\alpha \geqslant 0$ and $m = 1$. At several flow parameters, the energy growth of

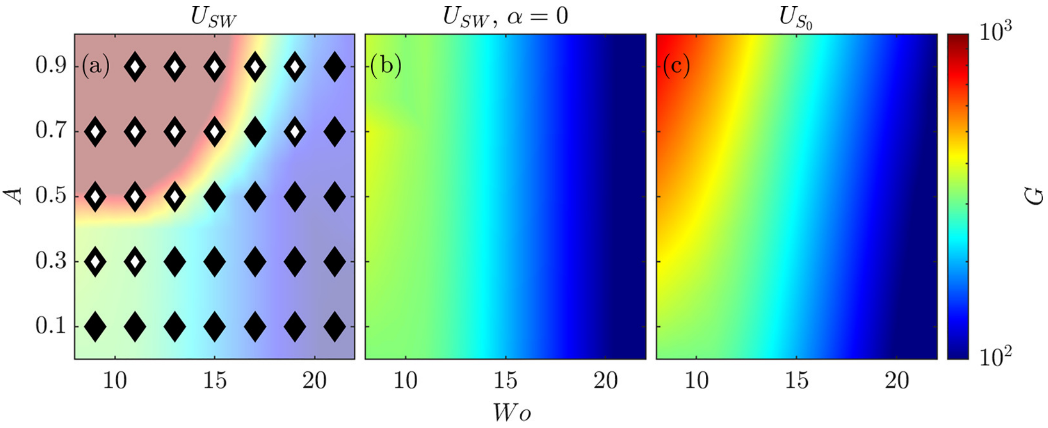

FIG. 5. With colors, the maximum transient energy growth of perturbations on top of master U_{SW} [(a) and (b)] and slave U_S (c) laminar profiles. Note that the color scale is limited to a maximum of $G \leqslant 10^3$ for clarity. The results correspond to different Wo and A at Re = 2100. In (a) the maximum energy growth of any helical or streamwise-constant perturbation with $\alpha \geqslant 0$ and $m = 1$ on top of U_{SW} profiles. The symbols correspond to DNS results in a $L = 100D$ long pipe initialized with a localized turbulent puff. Symbols denote pairs of DNS whose master simulation has puffs that survive for long times. Hollow symbols indicate pairs of DNS whose slave simulation has puffs that decay at $t \leqslant t_d = 120D/U$, while filled symbols indicate slave DNS where puffs survive for longer times. In (b), the maximum energy growth of streamwise-constant perturbations with axial $\alpha = 0$ and azimuthal $m = 1$ wave numbers on top of the U_{SW} profile. In (c) the maximum energy growth of any perturbation $\alpha \geqslant 0$ and $m = 1$ on top of the laminar slave U_S profile.

helical perturbations, with $\alpha > 0$, is much higher than for any other perturbation [21]. The flow parameters at which this happens can be clearly identified as the intense red region in Fig. 5(a). In the second TGA, we fix $\alpha = 0$ and $m = 1$ and compute the growth of streamwise-constant perturbations. According to our TGA, and as observed by Xu *et al.* [21], the SW profile is susceptible to the growth of streamwise-constant perturbations, see Fig. 5(b). Only at high Wo or small A is the growth of streamwise-constant perturbations larger than the growth of helical perturbations.

For slave profiles we perform just one TGA, in which we consider all possible perturbations with $\alpha \geqslant 0$ and $m = 1$. The results of this analysis are shown in Fig. 5(c). At all the flow parameters we consider here, the perturbations that reach the highest energy growth are streamwise-constant perturbations (with $\alpha = 0$ and $m = 1$). Note that their energy growth is similar to the ones obtained in the SW profile; compare Figs. 5(c) and 5(b). This confirms that our slave profiles qualitatively capture the transient growth characteristics of streamwise-constant perturbations in the SW profile. This growth is linked to the mean shear of the flow, as in SSPF, and not to the presence of inflection points [17]. It also shows that, unlike the actual SW profile, our slave profiles are not susceptible to the outstanding growth of helical perturbations.

B. Master-slave DNS

We perform pairs of master-slave DNS at several flow parameters. In each pair, both simulations are initialized with the same turbulent field, that has a (single) turbulent structure. The slave profiles have a shear that monotonically decreases from the center line to the pipe wall. However, by construction, the kinetic energy of the slave profiles matches the kinetic energy of the instantaneous master profile. The slave profiles are time dependent and do not have inflection points. They are also more blunted, the more deformed the corresponding master profiles are with respect to the SW profile; see Appendix A.

Find an example of the slave profiles, and their master counterparts, in DNS at $\text{Re} = 2100$, $\text{Wo} = 11$, and $A = 0.5$ in Figs. 4(e)–4(h). For this parameter set, the U_{SW} profile is susceptible to the growth of helical perturbations, as seen in Fig. 5(a), and, while the master simulation has a localized puff that survives for a long time, Fig. 6(c), the puff in the slave simulation decays in less than two pulsation periods, Fig. 6(d). At $A = 0.1$ and $\text{Wo} = 11$, see Figs. 6(a) and 6(b), both the slave and master profiles are not susceptible to the growth of helical perturbations, Fig. 5. At these parameters, puffs survive during the whole simulation time for both slave and master simulations.

In order to check whether this behavior is reproduced at other flow parameters, we set a heuristic time threshold at $t_d = 120D/U$ that corresponds to a time span of more than three pulsation periods for all cases considered here $t_d > 3T$. Our master-slave DNS are classified according to whether the slave simulation shows a decay event. See in Fig. 5(a) a graphic representation of this classification for different combinations of A and Wo at $\text{Re} = 2100$. Full symbols denote slave simulation in which the puff survives for long times. Hollow symbols indicate slave simulations that show puff decay at $t \leqslant t_d$. In all the cases the master simulation survives. There is a clear boundary between cases that show quick puff decay in the slave simulations and those which do not. At $A \gtrsim 0.5$ and $8 \lesssim \text{Wo} \lesssim 17$ pulsatile pipe flows are highly susceptible to the growth of helical perturbations, Fig. 5(a). As seen in Fig. 5(a), at these flow parameters, after suppressing the inflection points, puffs quickly decay in the corresponding slave DNS. At $A \lesssim 0.3$ and/or $\text{Wo} \gtrsim 20$, the growth of the helical perturbations is smaller than that of the streamwise-constant perturbations, see Fig. 5(a) compared to Fig. 5(b). At these flow parameters, eliminating the inflection points has no effect on the lifetime of turbulent puffs. This result further supports that, at certain Re, Wo, and A, as soon as puffs cannot make use of the inflection points to survive, they quickly decay.

V. EBM RESULTS

In this section we compare the DNS results with the EBM. The EBM includes two main changes compared to the BM. These changes are inspired by our analyses in the previous sections and model

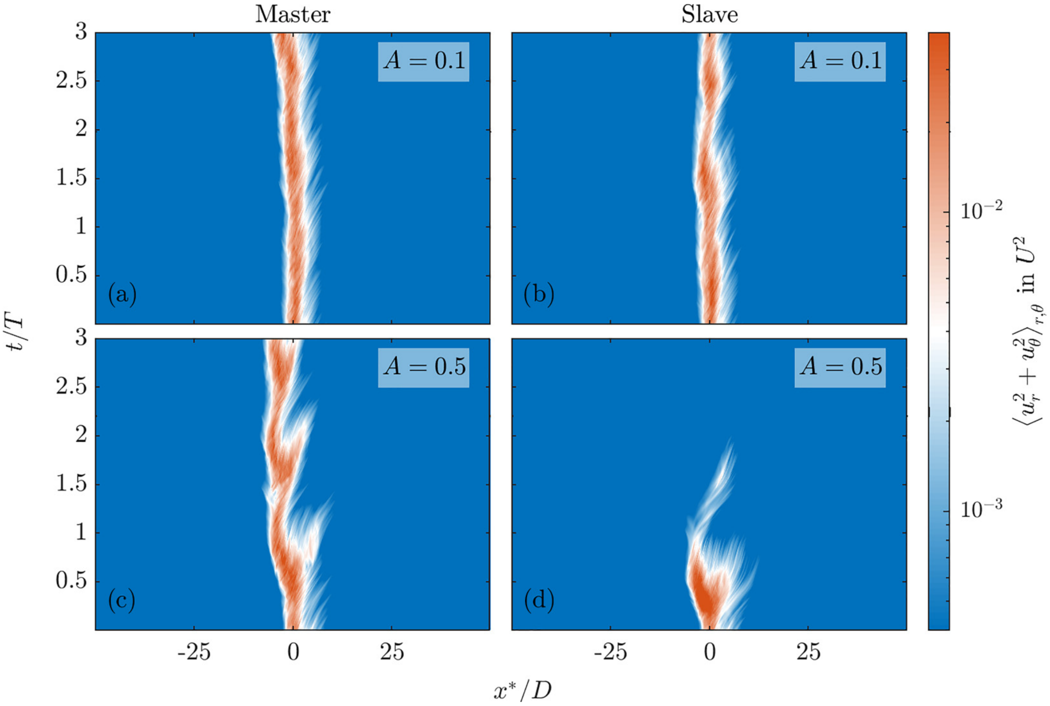

FIG. 6. Space-time diagrams of the cross-section integral of turbulent cross-section kinetic energy in master-slave DNS at $\mathrm{Re} = 2100$ and $\mathrm{Wo} = 11$ and two different A. The results correspond to two pairs of master-slave DNS in a $L = 100D$ long pipe initialized with a localized turbulent puff. The results are plotted with respect to a moving reference frame moving at the bulk velocity $\bar{U}$. Panels (a) and (c) correspond to master simulations and (b) and (d) to slave simulations.

the two turbulence production mechanisms discussed in this study. One is the phase-lagged effect of a time-varying mean shear and the other the linear instabilities due to the inflection points in the laminar profile. A detailed description of the EBM is in Appendix B.

In Fig. 7, we include three examples of DNS and EBM results comparisons. The model is able to capture reasonably well the turbulent front speed and turbulence behavior of all the cases, as seen qualitatively in Fig. 7. With only some exceptions, we observe a good agreement between the EBM and all the DNS listed in Tables I and (only master DNS) II.

A. Turbulence production in the EBM

In the EBM, there are two main sources of turbulence intensity q production, see Eq. (B9). One is the time-varying Re number that is modelled with the term $r\bar{U}(t + \phi)$, being ϕ a phase lag that only depends on Wo. The second one is the instability of the mean profile that is modelled by the product $\gamma\lambda(t)$. Here $\lambda(t)$ is the growth rate of the instantaneous instability of the laminar SW profile, as computed by Morón *et al.* [17] using a numerical method first developed by Meseguer *et al.* [3]. The parameter γ only depends on Re and Wo. Here we test the effect of ignoring these two mechanisms, one at a time. In Fig. 8 we show further comparisons between DNS and EBM results. We show results of the EBM model with the fitted parameters listed in Table III and also with either $\phi = 0$ or $\gamma = 0$ that is without phase lag or without inflectional instability.

At $\phi = 0$ the model results clearly differ from the DNS ones at most flow parameters; see Figs. 8(d) and 8(h). For instance, at $\mathrm{Re} = 3000$, $\mathrm{Wo} = 6$, and $A = 1$, our DNS shows rapid decaying puffs (RaD); see Fig. 8(a). However, at $\phi = 0$, the EBM returns an ever-elongating puff;

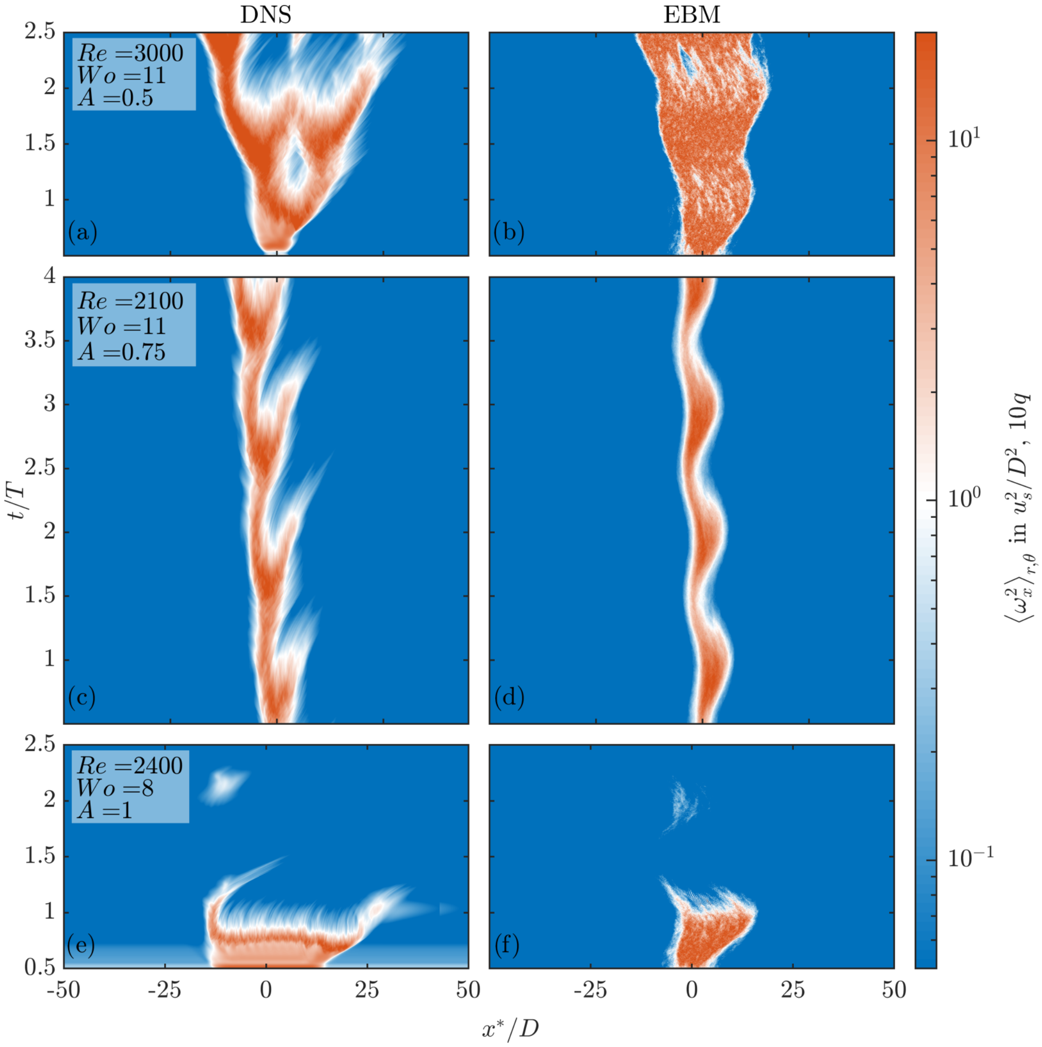

FIG. 7. Space-time diagrams of the cross-section integral of axial vorticity squared of DNS [(a), (c), and (e)] and $10q$ of the EBM [(b), (d), and (f)] in a $100D$ long pipe. The DNS are initialized with the optimal perturbation scaled to $|\mathbf{u}_0'| \approx 3 \times 10^{-2}$ of magnitude and localized in a span of $5D$ as in Ref. [24] and the model simulations with a localized perturbation of length $5D$. The figure is presented with respect to a moving frame x^*, moving with the bulk velocity $\bar{U}$. Panels (a) and (b) correspond to $\mathrm{Re} = 3000$, $\mathrm{Wo} = 11$, and $A = 0.5$. Panels (c) and (d) correspond to $\mathrm{Re} = 2100$, $\mathrm{Wo} = 11$, and $A = 0.75$. Panels (e) and (f) correspond to $\mathrm{Re} = 2400$, $\mathrm{Wo} = 8$, and $A = 1$. This last result is reproduced from Feldmann *et al.* [24].

TABLE III. BM parameters as described in Barkley *et al.* [6] and the value of parameters used in the EBM.

	R_0	R_1	ζ	D_q	σ	δ	ϵ
BM	1920	2250	0.79	0.13	$\leqslant 0.5$	0.1	0.2
EBM	1920	2250	0.79	0.13	$0.2 \leqslant \sigma \leqslant 0.85$	0.1	0.1

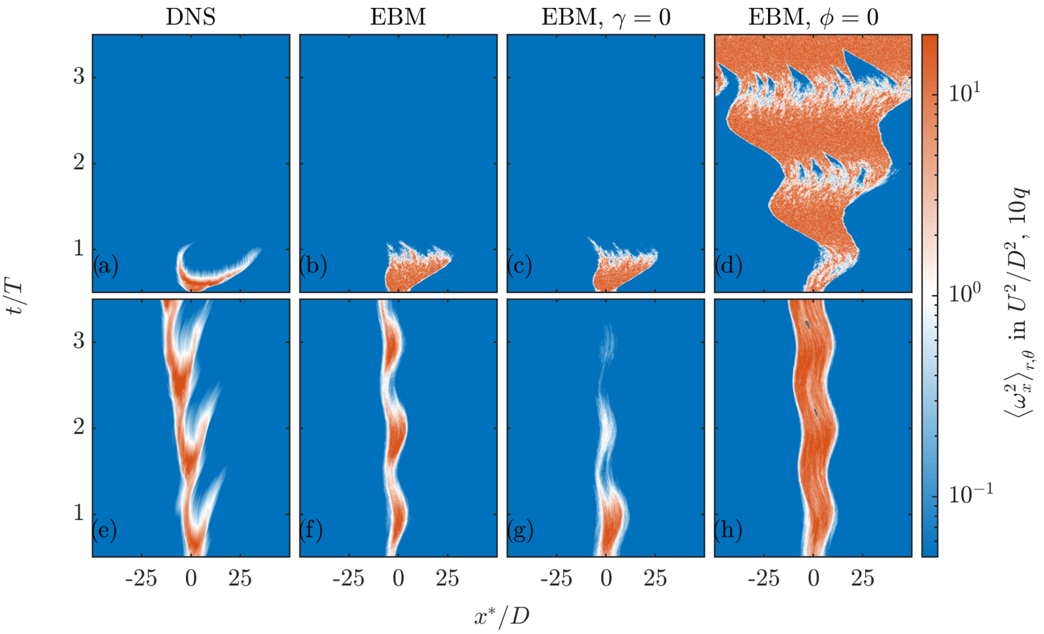

FIG. 8. Space-time diagrams of the cross-section integral of axial vorticity squared of DNS [(a) and (e)] and $10q$ of the EBM [(b), (c), (d), (f), (g), and (h)]. The results correspond to DNS and model simulations in a $100D$ long pipe at $A = 1$. The top panels [(a)–(d)] at $\mathrm{Re} = 3000$ and $\mathrm{Wo} = 6$. The bottom panels at $\mathrm{Re} = 2200$ and $\mathrm{Wo} = 11$. The DNS [(a) and (e)] are initialized with the optimal perturbation scaled to $|\mathbf{u}'_0| \approx 3 \times 10^{-2}$ of magnitude and localized in a span of $5D$ following Ref. [24], while the model simulations with a localized perturbation of length $5D$. The figure is presented with respect to a moving frame x^*, moving with the bulk velocity $\bar{U}$. Panels (b) and (f) correspond to EBM simulations with the fitted parameters listed in Table III. Panels (c) and (g) correspond to EBM simulations with the parameters listed in Table III but $\gamma = 0$. Panels (d) and (h) correspond to EBM simulations with the parameters listed in Table III but $\phi = 0$.

see Fig. 8(d). Moreover, at $\mathrm{Re} = 2200$, $\mathrm{Wo} = 11$, and $A = 1$, puffs are highly modulated by the pulsation in the DNS; see Fig. 8(e). However, if one sets $\phi = 0$, then in the EBM the behavior of the puff is less affected by the pulsation; see Fig. 8(h). Although we do not show it here, we see further divergences between model and DNS results at additional flow parameters when $\phi = 0$. This confirms that turbulence perceives the pulsation at a certain Wo-dependent phase lag with respect to the bulk velocity, as seen in Fig. 3(a), and also observed by Weng *et al.* [27] and other studies.

We also show results of the EBM with $\gamma = 0$, see Figs. 8(c) and 8(g). At $\mathrm{Re} = 3000$, $\mathrm{Wo} = 6$, and $A = 1$, there is no apparent effect of ignoring the linear instability of the mean profile, see Figs. 8(a) and 8(c). At these flow parameters turbulence rapidly decays due to the effect of the pulsation, regardless of the presence of inflection points in the profile. However, at $\mathrm{Re} = 2200$, $\mathrm{Wo} = 11$, and $A = 1$, while puffs remain localized in the DNS [see Fig. 8(e)], at $\gamma = 0$, puffs in the EBM quickly decay [see Fig. 8(g)]. This is similar to what we observe in our master-slave DNS shown in Fig. 5(c). At these flow parameters, without the inflection points and their corresponding linear instability, puffs quickly decay due to the effect of the pulsation.

According to our results with the EBM, one needs to include the phase lag ϕ and the effect of the instantaneous instability in the model to correctly approximate the behavior of puffs in pulsatile pipe flow.

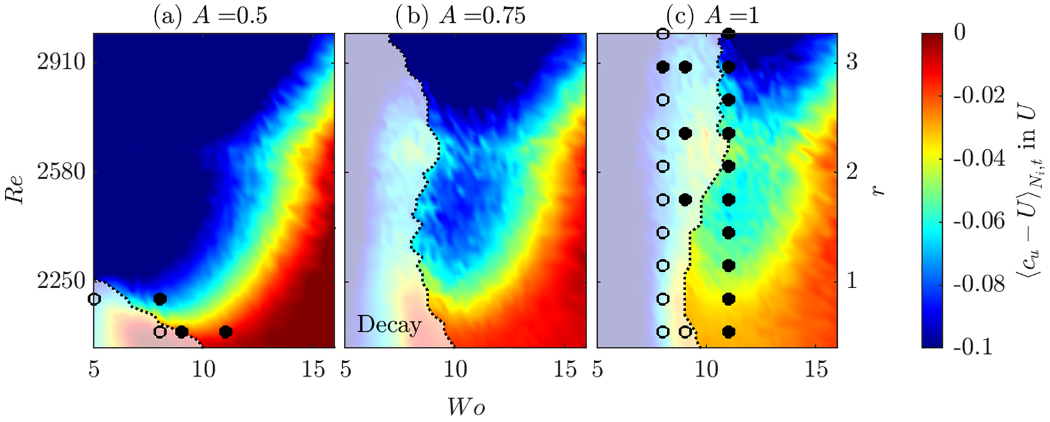

FIG. 9. With colors, time (t), and ensemble- (N_i) averaged upstream front speed c_u of q according to simulations of the EBM at several Re and Wo and at three different pulsation amplitudes: In (a) at $A = 0.5$, in (b) at $A = 0.75$, and in (c) at $A = 1$. Each panel corresponds to the interpolated results of an original set of 39×37 Re and Wo combinations. Each combination of Re and Wo has $N_i = 50$ individual simulations. The dotted lines denote the threshold between Re and Wo cases where more than half of the N_i simulations show turbulence decay, $\langle q\rangle_x \leqslant 0.01$, before $t/T < 4$. With black dots we denote the observed survive or decay behaviors of different DNS at parameters close to the decay threshold. Filled dots correspond to simulations where turbulence survives for long times or splits or elongates. Hollow points denote DNS where we observe turbulence decay at $t/T \leqslant 8$.

B. Parametric study using the EBM

We use the EBM to perform simulations in a large Wo and Re parametric space at three different amplitudes, $A = 0.5, A = 0.75$, and $A = 1$. At each A, we consider 39 equispaced Re values between $2050 \leqslant \mathrm{Re} \leqslant 3000$ and 37 Wo values between $5 \leqslant \mathrm{Wo} \leqslant 16$. For each combination of Wo, Re, and A we perform $N_i = 50$ EBM simulations for $t/T \leqslant 4$ and compute the time- and ensemble-averaged upstream front speed of turbulent patches, $\langle c_u - U\rangle_{N_i,t}$. We stop the simulations either at $t/T = 4$ or when turbulence decays in the whole domain, $\langle q\rangle_x \leqslant 0.01$.

We show the ensemble- and time-averaged upstream front speed of the EBM as a colormap in Fig. 9, together with an empiric threshold for q decay. The threshold separates the parametric regions where more than half of the N_i EBM simulations decay, at $t/T \leqslant 4$, from the rest. It can be understood as a critical $\mathrm{Re}_c(\mathrm{Wo}, A)$, up to which all modelled puffs are more likely to decay than survive. This critical Re_c highly depends on Wo and A. At low Wo, the system behaves more quasisteadily and puffs need a higher mean Re to survive the phases of the period where $\bar{U}(t + \phi) < U$. The amplitude A sets the minimum Re at each Wo [15]. As A increases, this minimum Re increases. At $A = 1$, independently of the selected $\mathrm{Re} \leqslant 3000$, puffs show a high chance to decay as long as $\mathrm{Wo} \leqslant 10$.

Regarding the upstream front speed, at high Wo and independently of the selected A, $\langle c_u - U\rangle_{N_i,t}$ decreases as Re increases. This is expected as the behavior of puffs at high Wo is similar to the behavior of puffs in SSPF and the upstream front speed of puffs in SSPF decreases for increasing Re [6]. As Wo decreases, at $10 \lesssim \mathrm{Wo} \lesssim 16$, $\langle c_u - U\rangle_{N_i,t}$ decreases. At these frequencies, $\gamma\lambda > 0$ for some phases of the period, which increases the q production. This effect, can be understood as an increase of Re, and therefore causes a lower averaged c_u. As A (and/or Re) increases, λ increases [17], which results in a lower upstream front speed for all the parameters considered here. At $\mathrm{Wo} \approx 10$ the system is close to the decay threshold discussed above. Puffs tend to accelerate as they decay, which explains the increase of $\langle c_u - U\rangle_{N_i,t}$ at these pulsation frequencies.

However, our results show that, as Wo further decreases, $\langle c_u - U\rangle_{N_i,t}$ decreases again. This is due to the way we initialize the EBM simulations. At $t_0 = T/2$ puffs tend to elongate since

$r\bar{U}(t+\phi) \geqslant 0$ and $\gamma\lambda \geqslant 0$. Therefore, during the initial phase of the EBM simulations, at Wo $\lesssim 8$ puffs first rapidly elongate ($c_u - U < 0$) and then quickly decay when $\bar{U}(t+\phi) < U$. Since the decay happens faster than the elongation, the averaged front speed is $\langle c_u - U < 0\rangle_{N_i,t}$.

C. Assessment of the EBM results

The EBM qualitatively captures the behavior of the upstream front speed observed in the DNS, as seen after comparing Fig. 9 with Fig. 3(b). As in the DNS, the upstream front speed in the EBM decreases for increasing Re and A, and, at high Wo, it approaches the values of the upstream front speed of puffs in SSPF. The quantitative values of the upstream front speed of model and DNS are also similar.

In Fig. 9(c), additionally we represent with symbols the survival or decay behaviors of the DNS listed in Table I, whose flow parameters are close to the decay thresholds of the EBM. Hollow symbols represent DNS where we observe puff decay at $t/T \leqslant 8$ and solid ones DNS that show turbulence survival for long times. The model approximates relatively well the minimum Wo at each Re and A, where turbulence does not decay after a short number of pulsation periods. The match between EBM and DNS results is better at smaller A, like $A = 0.5$ than at higher A. At $A = 1$, while the model has a threshold to decay close to Wo $= 10$, in the DNS the threshold seems to be closer to Wo $= 8$ and slightly change as Re increases.

The observed discrepancies between model and DNS results are rooted in the limitations of the EBM and the underlying BM which are described in detail in Appendix B 7.

VI. CONCLUSIONS

In this paper we study the behavior of turbulence in transitional pulsatile pipe flow at $2100 \leqslant \text{Re} \leqslant 3000$, $5 \leqslant \text{Wo} \leqslant 20$, and $0.5 \leqslant A \leqslant 1$. At these flow parameters, turbulence tends to first appear in the form of localized turbulent structures whose length and magnitude are modulated by the pulsation. We perform 71 DNS and identify different behaviors of these turbulent puffs. At some flow parameters the structures decay after one pulsation period, or after a short number of periods, but always at a fixed phase of the pulsation. At other flow parameters, they survive the pulsation and remain localized for asymptotically long times or randomly split until the flow reaches a highly intermittent state with localized turbulent patches that split or decay in a quiescent laminar flow.

By performing a causal analysis we show that, at certain flow parameters, these patches actively make use of the inflection points in the quiescent laminar profile, and their corresponding instabilities, to survive the pulsation.

Using the lessons learned from the DNS results and the results of our causal analysis, we adapt the BM to pulsatile pipe flow. The new EBM is able to qualitatively approximate the behavior of turbulent patches at all studied flow parameters. Specifically it reproduces reasonably well the behavior of turbulent front speeds in pulsatile pipe flow, including their dependence on Re, A, and Wo. It also approximates the thresholds of rapid turbulence decay in terms of Re, A, and Wo.

According to our DNS, causal analysis, and the EBM results, turbulence in pulsatile pipe flow at these flow parameters makes use of mainly two mechanisms to survive. The first mechanism is the turbulent production due to the mean shear, which is maximum in the phases of the period where the bulk velocity $\bar{U}(t+\phi) > U$. This production has a certain lag ϕ with respect to the pulsation, which is mainly set by Wo. The second mechanism is the instantaneous instability of the quiescent laminar SW flow. As long as puffs remain localized in pulsatile pipe flow, and surrounded by a quiescent laminar profile with inflection points, they can take advantage of this instability to increase the turbulent production at certain phases of the period.

As future steps, one could extend the analysis to higher Re and different pulsation waveforms. We expect that, as Re increases, nonlinear effects become more important, as reported by Pier and Schmid [30], in detriment to the mean shear and the effect of inflection points. In fact, as the turbulent fraction increases at high Re, the inflection points should play a smaller role in turbulence production. Also at higher Re recent studies show that the waveform of the pulsation has a big impact on the behavior of the system [31,32]. It would be interesting to determine the parametric thresholds where the behavior of turbulence in pulsatile pipe flow transitions from localized modulated puffs to fully turbulent, but statistically phase-dependent, flow.

ACKNOWLEDGMENTS

This work was funded by the German Research Foundation (DFG) through the research unit `Instabilities, Bifurcations and Migration in Pulsating Flow (FOR 2688)` under Grant No. 349558021, which is gratefully acknowledged. Computational resources were partially provided by the North German Supercomputing Alliance (HLRN), which are also gratefully acknowledged. The authors also appreciate many fruitful and inspiring discussions with the fluid modeling and simulation group at ZARM, in particular Dr. Feldmann and Dr. Vela-Martin for suggesting the use of a phase lag in the EBM. We also acknowledge J. Cela París for inspiring the small variations formulation we use to compute our slave profiles. Finally, the authors are grateful to Prof. Dr. D. Barkley for fruitful discussions and suggestions to improve the paper.

APPENDIX A: DETAILED DESCRIPTION OF MASTER-SLAVE DNS

In this Appendix we provide a detail derivation of the slave profile and the methods we use to integrate our master-slave DNS. Note that, in this Appendix, we normalize r using the radius R, and not the pipe diameter.

The slave profile is defined so it complies with a series of conditions.

1. Condition 1: Boundary condition

The slave profile must comply with the no-slip boundary condition and thus vanish at the wall,

$$U_S(r = R, t) = 0. \tag{A1}$$

2. Condition 2: Time dependency and maximum energy

The slave profile must be time dependent. Its bulk velocity $\bar{U}_S(t)$,

$$\bar{U}_S(t) = \frac{2}{R^2}\int_0^R U_S r dr, \tag{A2}$$

is set equal to

$$\bar{U}_S(t) = \sqrt{\frac{3E_L(t)}{2}}, \tag{A3}$$

where

$$E_L(t) = \frac{1}{\pi R^2}\int_0^{2\pi}\int_0^R \frac{1}{2}U_{\mathrm{SW}}^2 r dr d\theta \tag{A4}$$

as the kinetic energy of the laminar pulsatile pipe flow $U_{\mathrm{SW}}(r, t)$. With this condition we ensure that the energy of the profile is always equal or smaller than the corresponding laminar U_{SW} profile.

3. Condition 3: Monotonic shear

The average shear,

$$S = \frac{2}{R^2}\int_0^R \frac{1}{2}\left(\frac{\partial U_S}{\partial r}\right)^2 r dr, \tag{A5}$$

of the profile must be minimum. Given conditions (A1) and (A3), by minimizing S, we obtain profiles whose shear monotonically decreases from the wall to the center line of the pipe, without inflection points.

4. Laminar slave mean profile

The parabolic profile,

$$U_{S_0}(r,t) = 2\bar{U}_S(t)\left[1 - \left(\frac{r}{R}\right)^2\right], \tag{A6}$$

whose energy is exactly $E_L(t)$, i.e., complies with these three initial requirements. By dropping the time dependence of $\bar{U}_S$ and E_L in the notation and setting $R = 1$, one finds

$$\int_0^1 U_{S_0}^2 r dr = 4\bar{U}_S^2 \int_0^1 (1 - r^2)^2 r dr = 4\bar{U}_S^2\left[\frac{r^2}{2} - \frac{2r^4}{4} + \frac{r^6}{6}\right]_0^1 = \frac{4\bar{U}_S^2}{6} = E_L. \tag{A7}$$

In the case of turbulent flow, the energy of the mean profile is smaller than the laminar one [8]. To enforce this condition, and avoid introducing excess kinetic energy in the slave simulations we use an additional constraint.

5. Condition 4: Energy of the slave mean profile

The slave mean profile must have the same energy as the master mean profile,

$$\frac{2}{R^2}\int_0^R \frac{1}{2}U_S^2 r dr = E_M(t) = \frac{2}{R^2}\int_0^R \frac{1}{2}\langle u_x\rangle_{\theta,x}^2 r dr. \tag{A8}$$

If $E_M \equiv E_L$, then the flow in the master simulation is laminar, $U_S \equiv U_{S_0}$, and the energy of the slave mean profile will be maximum. Otherwise, $E_M < E_L$, and the resultant U_S is blunted, as seen in Fig. 4.

6. Method of small variations

We can express mathematically conditions (A3)–(A8) in a functional,

$$\mathcal{S} = 2\int_0^R \mathcal{L}(r, U_S, U_S')dr, \tag{A9}$$

to be minimized, where $U_S' = \frac{\partial U_S}{\partial r}$,

$$\mathcal{L} = \frac{1}{2}U'^2_S r + \lambda_L\left(U_S r - \frac{\bar{U}_S}{2R}\right) + \mu_L\left(\frac{1}{2}U_S^2 r - \frac{E_M}{2R}\right) \tag{A10}$$

is the Lagrangian, and λ_L and μ_L are two Lagrange multipliers. We have dropped the time dependence of $\bar{U}_S$, E_M, and U_S and therefore $\mathcal{L}$, λ_L, and μ_L in the notation for clarity.

From the method of small variations, one can find the function U_S that minimizes $\mathcal{L}$ by solving the Euler-Lagrange equation,

$$\frac{\partial \mathcal{L}}{\partial U_S} - \frac{\partial}{\partial r}\frac{\partial \mathcal{L}}{\partial U_S'} = 0. \tag{A11}$$

In this case, one finds

$$\lambda_L r + \mu_L U_S r - \frac{\partial}{\partial r}(rU_S') = 0, \tag{A12}$$

that, after rearranging, results in the partial differential equation,

$$\frac{\partial^2 U_S}{\partial r^2} + \frac{1}{r}\frac{\partial U_S}{\partial r} - \mu_L U_S = \lambda_L, \tag{A13}$$

with the boundary condition (A1),

$$U_S(r = R) = 0. \tag{A14}$$

The homogeneous part of Eq. (A13) can be turned into a modified Bessel's equation of order 0,

$$r^2\frac{\partial^2 U_S}{\partial r^2} + r\frac{\partial U_S}{\partial r} - \mu_L U_S r^2 = 0, \tag{A15}$$

being the modified Bessel's equation of order ν_B,

$$x^2 y'' + xy' - \big(a^2x^2 + \nu_B^2\big)y = 0, \tag{A16}$$

with solution

$$y(x) = AI_{\nu_B}(ax) + BK_{\nu_B}(ax). \tag{A17}$$

Here I_{ν_B} and K_{ν_B} are the modified Bessel functions of order ν_B of the first and second kind and A and B integration constants. After comparing Eq. (A15) with (A17), $a = \sqrt{\mu_L}$ and $\nu_B = 0$. The solution is written as

$$U_S = AI_0(\sqrt{\mu_L}r) + BK_0(\sqrt{\mu_L}r), \tag{A18}$$

since K_0 diverges at $r = 0$, $B = 0$. Regarding the particular solution, the constant $U_S = C$,

$$-\mu_L C = \lambda_L \rightarrow C = -\frac{\lambda_L}{\mu_L}, \tag{A19}$$

is tried, yielding

$$U_S = AI_0(\sqrt{\mu_L}r) - \frac{\lambda_L}{\mu_L}. \tag{A20}$$

One can determine the constant A from the boundary condition, at $r = R \equiv 1$, and find

$$U_S = \frac{\lambda_L}{\mu_L}\left[\frac{I_0(\sqrt{\mu_L}r)}{I_0(\sqrt{\mu_L})} - 1\right]. \tag{A21}$$

At each time step a Newton-Raphson method is used to find the correct μ_L and λ_L that allow U_S to fulfill conditions (A5) and (A8).

7. Computational setup of master-slave DNS

We initialize each pair of master-slave DNS with the same flow field. This flow field is the resultant field of a previous DNS at similar flow parameters, and has only one localized turbulent structure. In order to integrate simultaneously the master and slave simulations, our code performs the following substeps at each time step:

(1) The master simulation is integrated one time step.

(2) Using the instantaneous mean profile $U_M = \langle u_x\rangle_{\theta,x}$ of the master, it computes the instantaneous energy E_M, see Eq. (A8). In our pseudospectral code, $U_M = \langle u_x\rangle_{\theta,x}$, corresponds to the (0, 0) Fourier mode of the axial velocity.

(3) Using the corresponding laminar pulsatile pipe flow kinetic energy E_L it computes the desired $\bar{U}_S$, see Eq. (A3).

(4) It uses a Newton-Raphson method to compute the U_S profile, Eq. (A21), that complies with the desired $\bar{U}_S$ and E_M.

(5) It overwrites the mean profile of the slave simulation and imposes U_S instead. (In the code, it overwrites the $(0, 0)$ Fourier mode of the axial velocity of the slave simulation.)

(6) It integrates one time step the slave simulation, ignoring the evolution of its mean profile.

The pipe length. The artificial profiles U_S depend on the selected length of the pipe L. For an infinitely long pipe $L \rightarrow \infty$, with a single localized turbulent puff, the mean profile of the master simulation will tend to the laminar profile $\langle u_x \rangle_{\theta,x} \rightarrow U_{\text{SW}}$. This means that the energy of the mean profile $E_M \rightarrow E_L$ and therefore $U_S \rightarrow U_{S_0}$. The Newton-Raphson method works better as long as $E_M \approx E_L$. However the computational cost increases as the length of the pipe increases. A good compromise is found, by setting a length of $L = 100D$.

APPENDIX B: DETAILED DESCRIPTION OF THE EBM

In this Appendix we first describe the BM [6]. We then justify the changes we use to extend the BM to the EBM and we explain the methods by which we numerically integrate the EBM. At the end of this Appendix we also comment on the limitations of the EBM.

1. The original BM

The original BM considers two one-dimensional time-dependent variables $q(x,t)$ and $u(x,t)$ [33]. The former corresponds to the turbulence intensity at each axial location and time. According to Barkley *et al.* [6] q represents some form of the cross-section integral of the cross-section kinetic energy, so $q \geqslant 0$. The variable u is a proxy of the state of the mean shear at each axial location and time, represented by the axial center-line velocity in the model. The center-line velocity u is bounded between the bulk velocity $\bar{U} = 1$ and the laminar center-line velocity $U_c = 2$ so $1 \leqslant u \leqslant 2$. The evolution equations of q and u in the BM read [6]

$$\frac{\partial q}{\partial t} = -(u - \zeta)\frac{\partial q}{\partial x} + f(q,u) + D_q \frac{\partial^2 q}{\partial x^2} + \sigma \tau(t,x) q, \tag{B1}$$

$$\frac{\partial u}{\partial t} = -u \frac{\partial u}{\partial x} + g(q,u), \tag{B2}$$

with

$$f(q,u) = q[r + u - U_c - (r+\delta)(q-1)^2], \tag{B3}$$

$$g(q,u) = \epsilon(U_c - u) + 2\epsilon(\bar{U} - u)q. \tag{B4}$$

$\tau(t,x)$ is white Gaussian noise in space and time and

$$r = \frac{\text{Re} - R_0}{R_1 - R_0} \tag{B5}$$

is a control parameter that represents a rescaled Reynolds number. The parameter R_0 corresponds to the first Re at which puffs survive for long times $R_0 = 1920$. The parameter R_1 corresponds to the first Re at which puffs elongate into slugs $R_1 = 2250$.

Overall, the model has seven parameters: ζ, D_q, σ, δ, R_0, R_1, and ϵ. When correctly fitted, see Table III, the model perfectly reproduces the front speed of puffs and slugs in SSPF [6,10]. For a comprehensive description of the model and its underlying ideas, the reader is referred to Ref. [7] and references therein.

Timescale of the model. In order to compare the model and DNS or experiment front speeds, Barkley *et al.* [6] proposes the velocity scale difference,

$$\psi = 2(C_0 - C_1) = 0.28. \tag{B6}$$

Here C_0 is the front speed velocity of puffs at $\text{Re} = R_0$ and C_1 the front speed of puffs at $\text{Re} = R_1$.

This velocity scale difference can also be understood as a timescale difference between model and DNS or experiments. In particular, an advective time unit (D/U) in DNS or experiments, corresponds to $\psi = 0.28$ time units in the model. This scale difference is important for the pulsatile case, where a pulsation period of length $T = \frac{\pi \mathrm{Re}}{2\mathrm{Wo}^2}$ in advective time units in DNS or experiments, corresponds to a period of length $T^* = 0.28T$ in the model.

2. Equations of the EBM

In order to adapt the BM to pulsatile pipe flow we introduce several changes. The equations of the EBM read

$$\frac{\partial q}{\partial t} = -[u - \zeta \bar{U}(t)]\frac{\partial q}{\partial x} + f_{\mathrm{EBM}}(q, u) + D_q \frac{\partial^2 q}{\partial x^2} + \sigma(\mathrm{Re})\tau(t, x)q, \tag{B7}$$

$$\frac{\partial u}{\partial t} = -u\frac{\partial u}{\partial x} + g_{\mathrm{EBM}}(q, u), \tag{B8}$$

with

$$f_{\mathrm{EBM}}(q, u) = q\{r\bar{U}(t + \phi) + \gamma\lambda(t) + u - U_c(t) - [r\bar{U}(t + \phi) + \delta](q - 1)^2\}, \tag{B9}$$

$$g_{\mathrm{EBM}}(q, u) = \epsilon[U_c(t) - u] + 2\epsilon[\bar{U}(t) - u]q + P_G(t) + F_{v_0}(t), \tag{B10}$$

where $\bar{U}$, U_c, P_G, and F_{v_0} are the corresponding bulk velocity, the laminar center-line velocity, the pressure gradient, and the viscous force at the center line of the pipe. Note that, different to the BM, these quantities are time dependent. Moreover, ϕ corresponds to a phase lag between the turbulence intensity and the bulk velocity. The product of γ and λ models the effect of inflection points in the U_{SW} profile on q. In order to better fit the model results to the DNS results we set $\epsilon = 0.1$ and change σ depending on Re,

$$\sigma = \frac{6}{5}\frac{(\mathrm{Re} - 1933)}{1000}, \tag{B11}$$

with a lower limit of $\sigma \geqslant 0.2$, so there are always some stochastic behaviors, and an upper limit of $\sigma \leqslant 0.85$, so the stochastic term is never too dominant. In Table III, we list the parameter values we use for the EBM throughout the paper. In what follows we justify the changes introduced in the EBM.

3. Extensions to the *u* equations

In pulsatile pipe flow, the laminar center-line velocity $U_c(t)$ and bulk velocity $\bar{U}(t)$ are functions of time. While the bulk velocity is set by the pulsation, the evolution of $U_c(t)$ can be obtained from the NSE. First, we assume laminar flow, $u(r, \theta, x, t) \to (0, 0, U_{\mathrm{SW}}(r, t))$ and, from the NSE, obtain an equation for the evolution of the (SW) laminar profile:

$$\frac{\partial U_{\mathrm{SW}}}{\partial t} = P_G(t) + F_{\mathrm{visc}}(r). \tag{B12}$$

Here $P_G(t)$ is the pressure gradient that drives the flow at the desired bulk velocity $\bar{U}(t)$ and

$$F_{\mathrm{visc}}(r) = \frac{1}{\mathrm{Re}}\left(\frac{\partial^2 U_{\mathrm{SW}}}{\partial r^2} + \frac{1}{r}\frac{\partial U_{\mathrm{SW}}}{\partial r}\right) \tag{B13}$$

is the viscous forces. At the center line of the pipe $r \to 0$,

$$F_{v_0}(t) = \lim_{r\to 0} F_{\mathrm{visc}} = \lim_{r\to 0}\left[\frac{1}{\mathrm{Re}}\left(\frac{\partial^2 U_{\mathrm{SW}}}{\partial r^2} + \frac{1}{r}\frac{\partial U_{\mathrm{SW}}}{\partial r}\right)\right]. \tag{B14}$$

If one applies L'Hopital's rule to the limit in Eq. (B14), then

$$F_{v_0}(t) = \frac{2}{\mathrm{Re}}\frac{\partial^2 U_{\mathrm{SW}}}{\partial r^2}, \tag{B15}$$

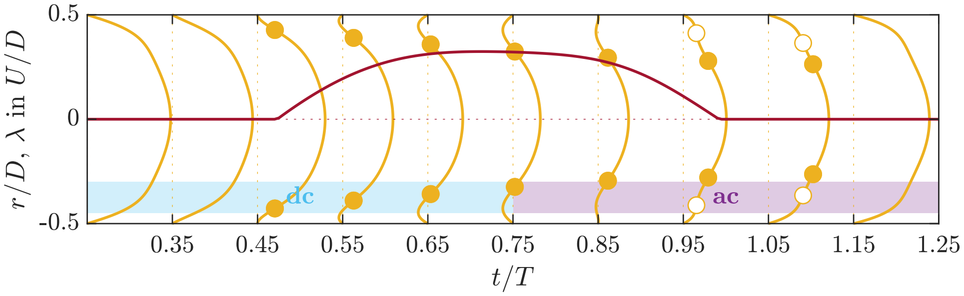

FIG. 10. Laminar profile and instantaneous maximum eigenvalue $\lambda_{\max}$ according the instantaneous stability analysis by Morón *et al.* [17]. In yellow the instantaneous laminar profiles U_{SW} at $\mathrm{Re} = 2100$, $\mathrm{Wo} = 11$, and $A = 0.9$. To not interfere with one another the profiles are scaled using a scalar with arbitrary units so the all time maximum is smaller than $t/T = 0.15$, since only the development of U_{SW} in time is of interest. With points find the existence and position r_i of inflection points in the profile. Filled points correspond to inflection points that also satisfy the Fjørtoft criterion locally $\frac{\partial^2 U_{\mathrm{SW}}}{\partial r^2}[U_{\mathrm{SW}} - U_{\mathrm{SW}}(r_i)] < 0$. In red, the parameter $\lambda = \max(0, \lambda_{\max})$ used in the EBM.

and, because $U_c(t) = U_{\mathrm{SW}}(t, r = 0)$,

$$\frac{\partial U_c}{\partial t} = P_G(t) + F_{v_0}(t). \tag{B16}$$

Note that the time average of the right-hand side of Eq. (B16) yields $\langle P_G(t) + F_{v_0}(t)\rangle_t = 0$. Therefore in the BM there is no need to consider these terms as they cancel each other at each time step. In the case of pulsatile pipe flow, however, the equilibrium of forces described in Eq. (B16) must be included in the model, see Eq. (B10).

4. Extensions to the *q* equations

In the original BM, Barkley *et al.* [6] assumed that the turbulence intensity is advected at the center-line velocity u, corrected with the parameter ζ. In the case of the EBM we multiply the parameter ζ in Eq. (B7) by the bulk velocity $\bar{U}$ to account for the effect of the pulsation. In the rest of this subsection we justify other changes to the evolution equations of q in the EBM.

a. Phase lag ϕ. In previous studies of pulsatile pipe flow, a phase lag between the driving bulk velocity and turbulence has been reported [27]. In our DNS we observe a time delay between the maximum integrated turbulence intensity $\langle \omega_x^2 \rangle_{r,\theta,x}$ and the bulk velocity $\bar{U}$ (see Fig. 3) that is mainly dependent on Wo. We find that, for the model purposes, the analytical phase lag $\phi(\mathrm{Wo}) \approx 32.34^\circ + 35.17^\circ \arctan[0.75(\mathrm{Wo} - 2)]$ between the pressure gradient and laminar profile, first derived by Womersley [14], is a good approximation to this phase difference.

b. The effect of the inflection points: λ and γ. At $5 \lesssim \mathrm{Wo} \lesssim 19$ and $A \gtrsim 0.5$, the laminar profile of pulsatile pipe flow is very different to the parabolic profile of the steady case and is instantaneously unstable at certain phases of the period [17]. The center-line velocity u alone is not able to capture these features of the mean shear. In the EBM the instantaneous shape of the mean shear and its effects are modeled by adding to Eq. (B9) the term $+\gamma\lambda(t)$.

Here $\lambda(t)$ represents how instantaneously linearly unstable the laminar profile is always $\lambda \geqslant 0$. We compute it using the method described in Morón *et al.* [17]. We compute the eigenvalues of the laminar profile at certain time steps as if the profile was instantaneously steady, using the method proposed by Meseguer and Trefethen [3]. We then assume that the maximum eigenvalue is continuous in time and construct $\lambda(t)$. We then force λ to be $\lambda \geqslant 0$. For more details the reader is referred to Morón *et al.* [17]. For an example of λ in the model, see Fig. 10. Note that, during the phases of the period where there are inflection points in the profile, λ is most of the time $\lambda > 0$.

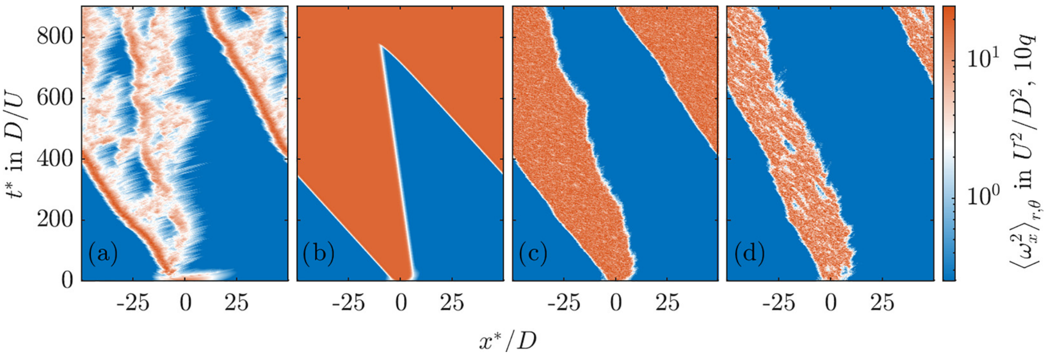

FIG. 11. Space-time diagrams of the cross-section integral of axial vorticity squared of DNS (a) and $10q$ of the BM [(b), (c), and (d)]. The results correspond to DNS and BM simulations in a $100D$ long pipe, at $\mathrm{Re} = 2400$, initialized with a localized perturbation of length $5D$. The figure is presented with respect to a moving frame x^*, moving with the bulk velocity $\bar{U}$, and time t^* in advective time units for DNS, and model units for the BM. Subplot (b) corresponds to a simulation of the BM with the parameters listed in Table III and $\sigma = 0$; (c) $\sigma = 0.5$ and (d) $\sigma = 0.7$.

The parameter γ sets the effect λ has on the growth of q in Eq. (B9). It models the quality of the quasisteady assumption used to compute λ. It scales with the length of the period in terms of flow units $T = \frac{\pi \mathrm{Re}}{2\mathrm{Wo}^2}$. The idea is that the longer the period is, the slower the mean shear evolves with respect to the turbulent structures. We find a good compromise with

$$\gamma = \min\left[1, 0.28 \log\left(T\right)\right]. \tag{B17}$$

We impose an upper boundary of $\gamma = 1$ so the dynamics of the model are not dominated by $\gamma\lambda$.

c. The noise intensity σ. The original BM does not capture all the chaotic behaviors of localized turbulence in the Re regime at $2250 \lesssim \mathrm{Re} \lesssim 2500$. In this regime, according to the BM, puffs elongate into slugs filling the whole pipe with turbulence, as seen in Figs. 11(b), 11(c) and 11(d). However, in full DNS, at these Re the flow usually reaches a highly heterogeneous state, where localized turbulent patches coexist with laminar flow patches; see Fig. 11(a). This behavior can only be approximated by radically increasing the noise parameter σ in the model, see Fig. 11(d), but at the same time losing the good agreement between model and DNS or experiments front speeds.

This limitation of the BM turns out to be even more detrimental in the case of the EBM as Re increases. We find that a noise intensity σ that scales linearly with Re in Eq. (B11) produces better results. The parameter has a lower bound so the model has some degree of stochastic behavior at low Re and an upper bound so the noise term is never more dominant than the rest of the dynamics of the model.

d. The parameter ϵ. In the original work of Barkley [7], they suggest that ϵ should be inversely proportional to Re. But, since changing this parameter does not have a huge impact on turbulence front speeds and survival in the case of SSPF, they keep it constant. In the case of pulsatile pipe flow, in order to find a better match with the DNS results, it should be slightly decreased. This is justified since, the maximum $\mathrm{Re}_{\max} = (1 + A)\mathrm{Re}$ is, in the worst-case scenario, two times the mean Re. Therefore ϵ is set to half its BM value in the EBM, see Table III.

5. Computational setup of the EBM

Equations (B7) and (B8) are integrated following Barkley *et al.* [6]. The second-order derivatives are discretized with second-order central finite differences and the first-order derivatives with a first-order upwind scheme. The system is integrated using an explicit Euler method, with a time-step size $\Delta t = 0.0025$. The results here correspond to a pipe of length $L = 100$ and a uniform grid spacing $\Delta x = 0.5$. The stochastic term is modelled as white Gaussian noise in space and time. All the EBM simulations are initialized with a localized $5D$ long disturbance with magnitude $q \leqslant 0.5$ at the initial time $t_0 = T^*/2$.

In order to prepare all the variables needed to integrate the EBM the following algorithm has been implemented. After selecting the desired A, Re, and Wo the code first numerically integrates the corresponding laminar profile to obtain all the time-dependent parameters: $\bar{U}$, U_c, P_G, F_{v_0}, and λ. It then computes the phase shift angle $\phi(\mathrm{Wo})$ and the parameter σ using Eq. (B11) and scales the pulsation period to adapt it to the timescale of the model using Eq. (B6). Finally, it integrates Eqs. (B7), (B8), (B9), and (B10).

6. The EBM at $A = 0.0$

Note that if one sets $A = 0$ in the EBM, except for the new definitions of σ and ϵ, then one recovers the original BM. At $A = 0$ the parameters derived from the laminar flow are constant in time: $U_c = 2$, $\bar{U} = 1$, $P_G + F_{v_0} = 0$, and $\lambda = 0$ and the EBM Eqs. (B7)–(B10) return to the BM Eqs. (B1)–(B4).

7. Limitations of the EBM

When correctly fitted the EBM captures the dynamics of pulsatile pipe flow in a broad parametric regime, but it has some limitations that need to be mentioned. Some of its limitations are inherited from the original BM. One is the intermittent behavior of turbulence at some flow parameters that is only captured if σ is scaled with Re. The other is the magnitude of q in the core of the slugs that the BM tends to overestimate [7]. This results in some qualitative differences in the structures observed in the model and the DNS.

New to the EBM is the sensitivity to the parameter γ. The EBM is expected to work worse as A increases. At higher A, and $\mathrm{Wo} > 5$, the laminar profile is very different to the simple parabolic profile of steady pipe flow, see Fig. 10, and the state of the mean shear can no longer be captured with one variable u. Here, instead of introducing more variables in the analysis, we find a a workaround by using the instantaneous linear instability λ and the parameter γ. Both work reasonably well, as long as γ is correctly fitted. But as soon as γ is changed, puffs either decay or elongate when they should not.

Also, due to the definition of γ the model overestimates the lifetime of puffs at certain flow parameters. In particular, according to the EBM, puffs at $10 \lesssim \mathrm{Wo} \lesssim 15$, $A = 1$, and $1800 \lesssim \mathrm{Re} \lesssim 2050$ survive the pulsation. This is obviously not observed in DNS of pulsatile pipe flow, where at $\mathrm{Re} \leqslant 2000$ and $A = 1$ puffs tend to decay independently of the pulsation frequency [17]. Moreover, at these flow parameters, the EBM is clearly dominated by the parameter λ and therefore by γ. We do not show it here as we do not consider these flow parameters in our analysis, but we believe it to be fair to at least mention these errors.

The EBM considers that, as long as $\lambda > 0$, turbulence can always make use of the instantaneous linear instability to grow. However, this may not be the case in a full DNS. At a given time step, the mean profile of a DNS can be highly perturbed. In this case, puffs would not have the chance to take advantage of the linear instability to grow and could even decay. This feature should be considered in future versions of the model.

---

[1] O. Reynolds, An experimental investigation of the circumstances which determine whether the motion of water shall be direct or sinuous, and of the law of resistance in parallel channels, Philos. Trans. R. Soc. **174**, 935 (1883).

[2] M. Avila, D. Barkley, and B. Hof, Transition to turbulence in pipe flow, Annu. Rev. Fluid Mech. **55**, 575 (2023).

[3] A. Meseguer and L. N. Trefethen, Linearized pipe flow to Reynolds number 10^7, J. Comput. Phys. **186**, 178 (2003).

[4] B. Eckhardt, T. M. Schneider, B. Hof, and J. Westerweel, Turbulence transition in pipe flow, Annu. Rev. Fluid Mech. **39**, 447 (2007).

[5] P. Schmid and D. Henningson, *Stability and Transition in Shear Flows*, Applied Mathematical Sciences (Springer, New York, 2000).

[6] D. Barkley, B. Song, V. Mukund, G. Lemoult, M. Avila, and B. Hof, The rise of fully turbulent flow, Nature London **526**, 550 (2015).

[7] D. Barkley, Theoretical perspective on the route to turbulence in a pipe, J. Fluid Mech. **803**, P1 (2016).

[8] J. Kühnen, B. Song, D. Scarselli, N. B. Budanur, M. Riedl, A. P. Willis, M. Avila, and B. Hof, Destabilizing turbulence in pipe flow, Nat. Phys. **14**, 386 (2018).

[9] B. Song, D. Barkley, B. Hof, and M. Avila, Speed and structure of turbulent fronts in pipe flow, J. Fluid Mech. **813**, 1045 (2017).

[10] K. Chen, D. Xu, and B. Song, Propagation speed of turbulent fronts in pipe flow at high Reynolds numbers, J. Fluid Mech. **935**, A11 (2022).

[11] A. Frishman and T. Grafke, Mechanism for turbulence proliferation in subcritical flows, Proc. R. Soc. A **478**, 20220218 (2022).

[12] F. Romanò, A. Charles, F. Dottori, and S. Amir Bahrani, Transition to turbulence in a heated non-Newtonian pipe flow, Phys. Fluids **33**, 091702 (2021).

[13] T. Sexl, Über den von E. G. Richardson entdeckten "Annulareffekt," Z. Phys. **61**, 349 (1930).

[14] J. R. Womersley, Method for the calculation of velocity, rate of flow and viscous drag in arteries when the pressure gradient is known, J. Physiol. **127**, 553 (1955).

[15] D. Xu, S. Warnecke, B. Song, X. Ma, and B. Hof, Transition to turbulence in pulsating pipe flow, J. Fluid Mech. **831**, 418 (2017).

[16] D. Xu and M. Avila, The effect of pulsation frequency on transition in pulsatile pipe flow, J. Fluid Mech. **857**, 937 (2018).

[17] D. Morón, D. Feldmann, and M. Avila, Effect of waveform on turbulence transition in pulsatile pipe flow, J. Fluid Mech. **948**, A20 (2022).

[18] S. J. Cowley, High frequency Rayleigh instability of stokes layers, in *Stability of Time Dependent and Spatially Varying Flows* (Springer, Berlin, 1987), pp. 261–275.

[19] J. R. Nebauer, On the stability and transition of time-periodic pipe flow, Doctoral dissertation, Ph.D. thesis, Monash University, 2019.

[20] D. Xu, A. Varshney, X. Ma, B. Song, M. Riedl, M. Avila, and B. Hof, Nonlinear hydrodynamic instability and turbulence in pulsatile flow, Proc. Natl. Acad. Sci. USA **117**, 11233 (2020).

[21] D. Xu, B. Song, and M. Avila, Non-modal transient growth of disturbances in pulsatile and oscillatory pipe flows, J. Fluid Mech. **907**, R5 (2021).

[22] B. Pier and P. J. Schmid, Optimal energy growth in pulsatile channel and pipe flows, J. Fluid Mech. **926**, A11 (2021).

[23] J. Kern, M. Beneitez, A. Hanifi, and D. Henningson, Transient linear stability of pulsating poiseuille flow using optimally time-dependent modes, J. Fluid Mech. **927**, A6 (2021).

[24] D. Feldmann, D. Morón, and M. Avila, Spatiotemporal intermittency in pulsatile pipe flow, Entropy **23**, 46 (2021).

[25] J. M. López, D. Feldmann, M. Rampp, A. Vela-Martín, L. Shi, and M. Avila, nscouette – A high-performance code for direct numerical simulations of turbulent Taylor–Couette flow, SoftwareX **11**, 100395 (2020).

[26] A. P. Willis, The openpipeflow Navier–Stokes solver, SoftwareX **6**, 124 (2017).

[27] C. Weng, S. Boij, and A. Hanifi, Numerical and theoretical investigation of pulsatile turbulent channel flows, J. Fluid Mech. **792**, 98 (2016).

[28] F. Tuerke and J. Jiménez, Simulations of turbulent channels with prescribed velocity profiles, J. Fluid Mech. **723**, 587 (2013).

[29] A. Vela-Martín, The synchronisation of intense vorticity in isotropic turbulence, J. Fluid Mech. **913**, R8 (2021).

[30] B. Pier and P. J. Schmid, Linear and nonlinear dynamics of pulsatile channel flow, J. Fluid Mech. **815**, 435 (2017).

[31] M. C. Brindise and P. P. Vlachos, Pulsatile pipe flow transition: Flow waveform effects, Phys. Fluids **30**, 015111 (2018).

[32] D. Scarselli, J. M. Lopez, A. Varshney, and B. Hof, Turbulence suppression by cardiac-cycle-inspired driving of pipe flow, Nature London **621**, 71 (2023).

[33] D. Barkley, Simplifying the complexity of pipe flow, Phys. Rev. E **84**, 016309 (2011).